Simulations of SNO during an Air or Partial Fill

S.D. Biller, M.E. Moorhead, D.L. Wark

University of Oxford

April 14, 1997

SNO–STR–97–011

1 Summary and Conclusions

The purpose of this document is to outline what we can expect to learn from an air fill of the SNO detector. All of the topics outlined in this report could use more analysis, but the hope is that this report will provoke discussion and demonstrate that the air fill data is of great interest to the SNO collaboration. Our conclusion is that every effort should be expended to guarantee that the detector will be ready to take believable data while it is still filled with air. Of course we are limited to those predictions that can be made from the SNOMAN Monte Carlo, and one should always remember that the most interesting things we learn will probably be those which we have not predicted.

If anyone tries to reproduce the detailed results in this report they should note that the muon results were generated with the new muon code from SNOMAN 3_00 installed in SNOMAN 2_09 (thus there would be ≈10 hits/MeV from an electron within the D_2O in the code used for the muon results), while all the other results were generated with an intermediate version of SNOMAN 3_00 which produces a very low number of hits/MeV (6.7 hits/MeV for 5 MeV electrons within the D_2O). This should not affect any of the conclusions, as it will simply shift the results down the NHIT axis, but it will mean that anyone trying this at home will probably generate more hits for some of the tests described here.

To start at the end, our conclusions are:

- 1. Simulations (outlined below) make definite, specific predictions about the performance of the SNO detector in air which can be checked against the data. The predictions include sharp features free from confusing effects which stand well clear of backgrounds. These features thereby will provide strong tests of both detector performance and the quality of the simulation. Verifying at this point that the detector is working as expected has a number of advantages. Firstly, there may be problems which could be rectified while the detector is filled with air that will become difficult to repair once it is filled with water. Secondly, the earlier we find out about problems the smaller the effect they may have on the schedule for meeting SNO's main objectives. Thirdly, demonstrating that the detector works as expected at the air fill stage will guarantee that we can use the first water fill data for physics analysis. This should allow us a clean radon data sample. Lastly, all four of the

topics considered in detail in this report yielded tests which are of physics interest to SNO which cannot be replicated once the detector is filled with water.

- 2. Reflection peaks in laserball data, which can only be seen during air fill, would provide a unique and highly sensitive test of the detector geometry and the optical transport modelling. These peaks could also be used to check PMT channel mapping and provide an independent check on acrylic attenuation lengths. These attenuation lengths would also be measured based on the observed intensity of direct light to an accuracy of better than 5%, independent of potential complications due to attenuation/scattering in either D2O or H2O.

- 3. Locally (fast) triggered gamma ray sources, such as the ^{16}N source, will produce detectable events from Compton scattering in the AV. These events can be used to calibrate SNO's NHIT energy spectrum for the air fill. Since the optical properties of the AV will have been independently measured (see above), this energy calibration can be used to determine the absolute PMT counting efficiencies to an accuracy of about 5%. It should be noted that there will be a further systematic error of order 5% in relating the absolute efficiency of PMTs in air to that of the same PMTs immersed in water which comes (mainly) from uncertainties in photocathode thickness [2].

- 4. Muons penetrating the AV while it is filled with air produce a pronounced peak in the NHIT distribution which is well clear of any background. This peak could produce a statistically significant test of the absolute photon counting efficiency of the SNO detector in air with only a few days of data. A number of obvious systematics have been checked and so far it appears likely that this measurement could be performed with an uncertainty of around 5%. Comparison of this measurement with the ^{16}N measurement will produce a valuable check on the analysis and Monte Carlo.

- 5. The flux of high energy gammas (> 4 MeV) from the cavity walls can be measured with high statistical accuracy with one day of SNO data when the AV is half-full of D_2O. Systematic errors in this measurement, and how it can be used to predict the gamma flux that will reach SNO's fiducial volume once it is filled, have not been carefully studied, but an error of a factor 2 in the final answer seems reasonable. These systematic errors will be different to those of Ref. [1] which is a complementary measurement of the cavity gamma flux.

Contents

1 Summary and Conclusions 1

2 Optical calibration in Air 4
- 2.1 Reflection Peaks 4
- 2.2 Direct Light 6

3 Detector Response to Gammas 9
- 3.1 Air Fill 9
  - 3.1.1 Test of ^{16}N Calibration System 9
  - 3.1.2 External Gammas from the Rock 12
- 3.2 Half Fill 17
  - 3.2.1 ^{16}N Calibration Source 17
  - 3.2.2 External Gammas 20

4 Detector Response to Muons 25

2 Optical calibration in Air

2.1 Reflection Peaks

Differences in the refractive indices between air and acrylic will cause a fraction of the incident light to be reflected from each boundary separating these media. For a light source placed within the spherical AV shell, this causes a portion of the light to be focussed towards the hemisphere opposite to that in which the light source is placed. The position of the observed focussed light clearly depends on the specific shape of the AV and PSUP. The prediction of this focussing therefore serves as an excellent check of detector geometry as well as the optical transport within SNOMAN. In addition, since about half of the reflected photons are reflected from the outer AV/air interface, these photons involve two additional transits through the acrylic. Consequently, the observed intensity of the focussed light is very sensitive to the acrylic attenuation length.

To illustrate this effect, SNOMAN simulations were run for lightball positions along the detector axis at z=0, 1, 2, 3, 4 and 5 meters above the equator. The lightball intensity was set below the single pe level and the total number of hits were recorded in each PMT after 1000 triggers for each configuration. The lightball wavelength was taken to be 337nm, corresponding to the fundamental wavelength of the nitrogen laser and lying just below the edge of the acrylic absorption spectrum. This procedure was repeated for the cases of "normal" air-fill data, air-fill data with the acrylic attenuation turned off, and water-fill data with the acrylic attenuation turned off. For each of these cases, the average number of hits per PMT was plotted as a function of $\cos\theta$, where θ is the PMT angle with respect to nadir (*i.e.* $\cos\theta$=1 points towards the bottom of the detector). Figure 1 shows the results for lightball positions z=0 - 5 meters. Note that the water-fill simulation also involves attenuation in the water which reduces the observed light level to approximately that of the air-fill case with acrylic attenuation.

For the z=0 case, as expected, all distributions are flat. As the lightball is moved upwards, the relative intensity in the upper hemisphere increases due to the proximity of these tubes to the source. In addition, a peak appears in the forward direction of the lower hemisphere when z=2. It grows at z=3 and then broadens and shifts for z=4 and 5 meters. In figure 2, the air-fill simulation with acrylic attenuation is normalized to the case with no attenuation for the z=4 meters configuration. This demonstrates the fact that the relative height of the reflection peak is strongly dependent on the acrylic attenuation. This suggests that the extent of the acrylic attenuation might be extracted purely from the shape of the reflection distribution, thus providing an independent determination of this important parameter. Furthermore, since the reflections produce a well-defined ring which moves toward the equator as the lightball is moved upwards, groups of tubes can be checked for the consistency of the geometric mapping of their electronic channels. In fact, by moving the light source along a perpendicular axis as well (*i.e.* in the equatorial plane), individual PMT channels could be isolated.

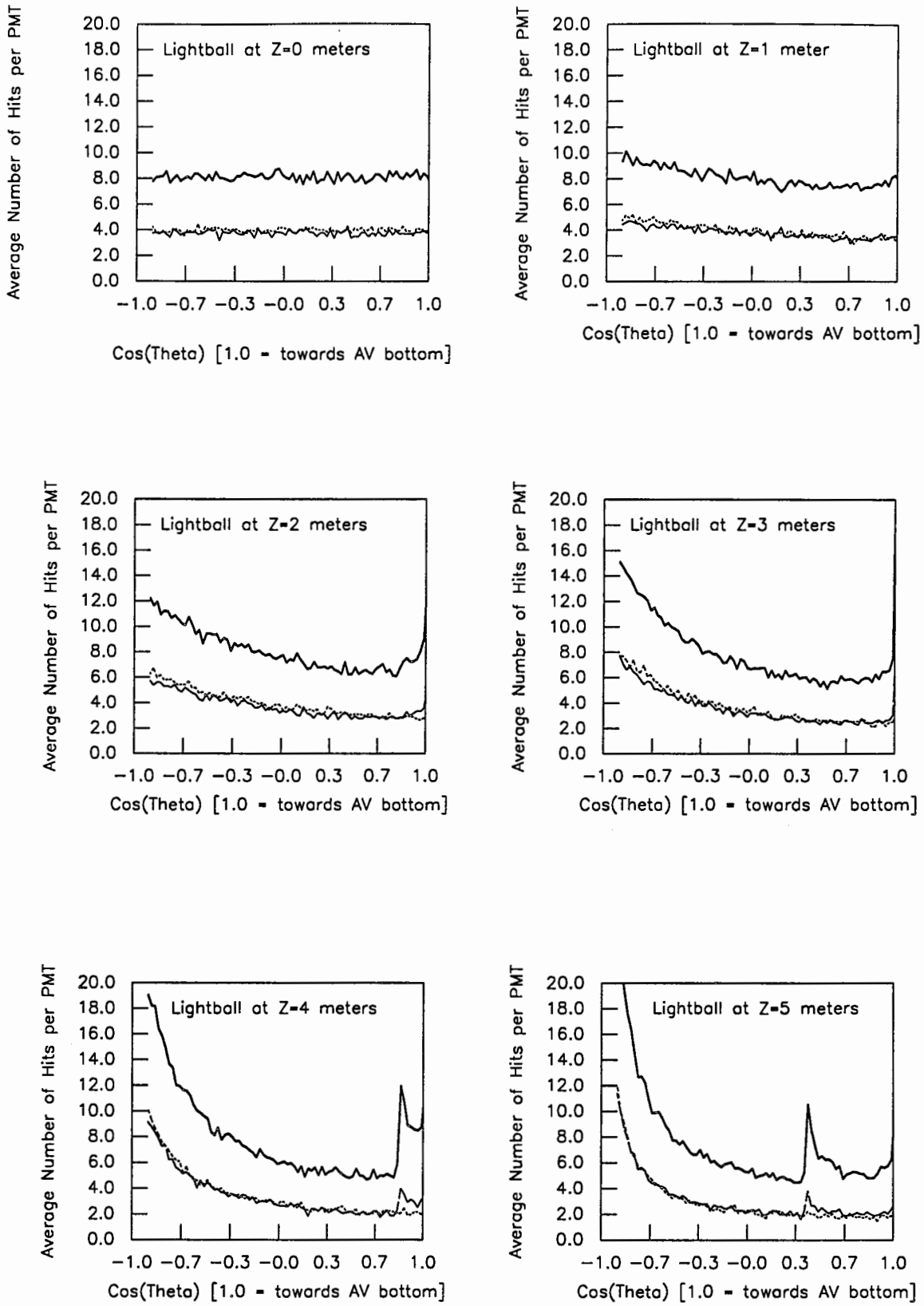

Figure 1: Variation in PMT rate as the light ball is moved up the z axis. Upper solid line = air fill, no acrylic attenuation; lower solid line = air fill with acrylic attenuation, dots = water fill, no acrylic attenuation

Note that in all these cases no forward peak structure is seen for the water-fill simulation. This is because indices of refraction of water and acrylic are sufficiently close that the reflection effects are significantly reduced. Consequently, any information which can be gained by studying these focussing effects will be lost unless air-fill data is taken.

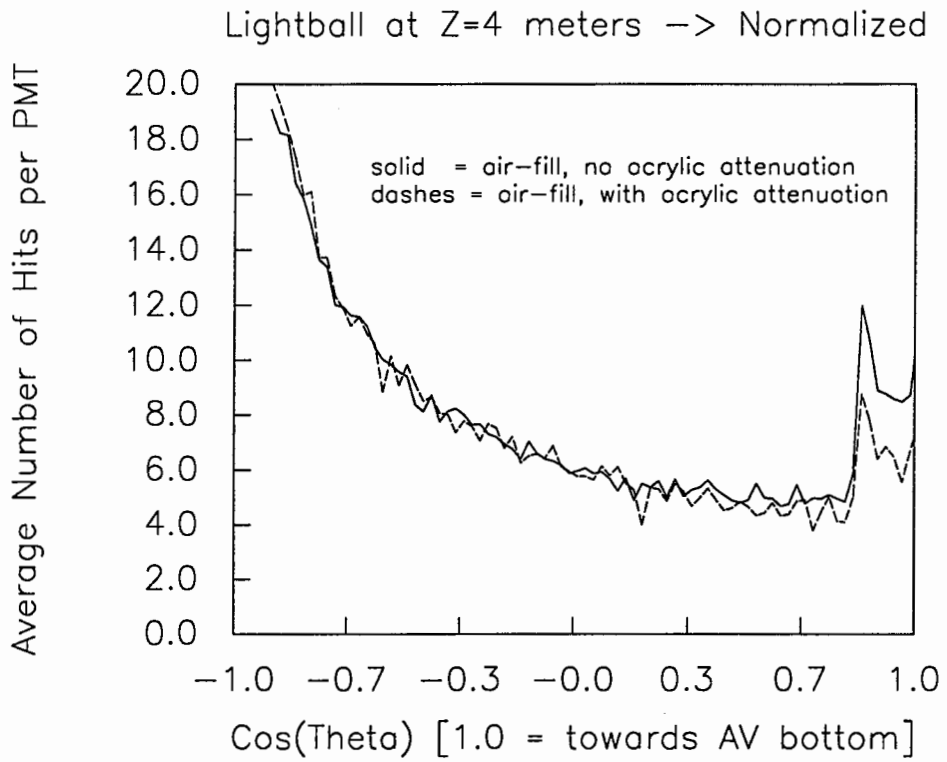

Figure 2: Normalized lightball curve at z=4 meters for airfill with and without acrylic attenuation.

2.2 Direct Light

For PMTs positioned around the AV equator, figure 3 shows the total number of hits (for 300 tubes) as a function of the lightball position along the z-axis for a variety of simulation configurations. Those cases involving attenuation in either acrylic or water obviously result in a lower observed light level which can be easily determined with respect to a single measurement taken with the lightball positioned outside the AV. The air-fill data thus offers the opportunity to easily determine the acrylic attenuation independent of the effects of attenuation in light and heavy water. In practice, this optical calibration would be accomplished by first comparing the observed light levels in a set of tubes for both lightball positions (*i.e.* inside and outside the AV) at wavelengths above 400nm. Here, all acrylic panels transmit $\sim 90 \pm 2\%$ of the light, so that the relative intensities can be used to account for geometric factors at about the 2% level. The change in this relative intensity at lower wavelengths may then be attributed to acrylic attenuation. The statistical uncertainty in the relative intensity measurement will be $\sim$1% and the location of the lightball inside the AV will be known to about 5cm, yielding a further systematic

uncertainty of about 1.5%. The acrylic attenuation lengths should thus be measured to better than 5%.

In figure 4, the curves are normalized at the z=0 position and the effect of line-of-sight solid angle is taken out. Note that for those configurations involving no attenuation, this results in a flat distribution both for air-fill and water-fill data. This demonstrates that the geometric corrections are, indeed, fairly straight-forward. This also indicates that effects due to the angular response of the PMT/reflector are very small as are reflection and refraction from the AV in this case. Consequently, measurements made during an air-fill can be directly related to the expected distributions for water-fill data with little extrapolation needed. Note also that from the shape of this curve, attenuation due to the acrylic and/or water becomes noticeable for lightball positions z=4 and 5 meters (corresponding to angles of 25 and 30 degrees with respect to the PMT orientation). However the medium responsible for this attenuation cannot be determined from this curve alone. Therefore measurements of the acrylic attenuation made during an air fill would be very useful for separating the effects of attenuation in the different media during a subsequent water fill (although measurements inside and outside the AV during the water fill could also be used for this purpose).

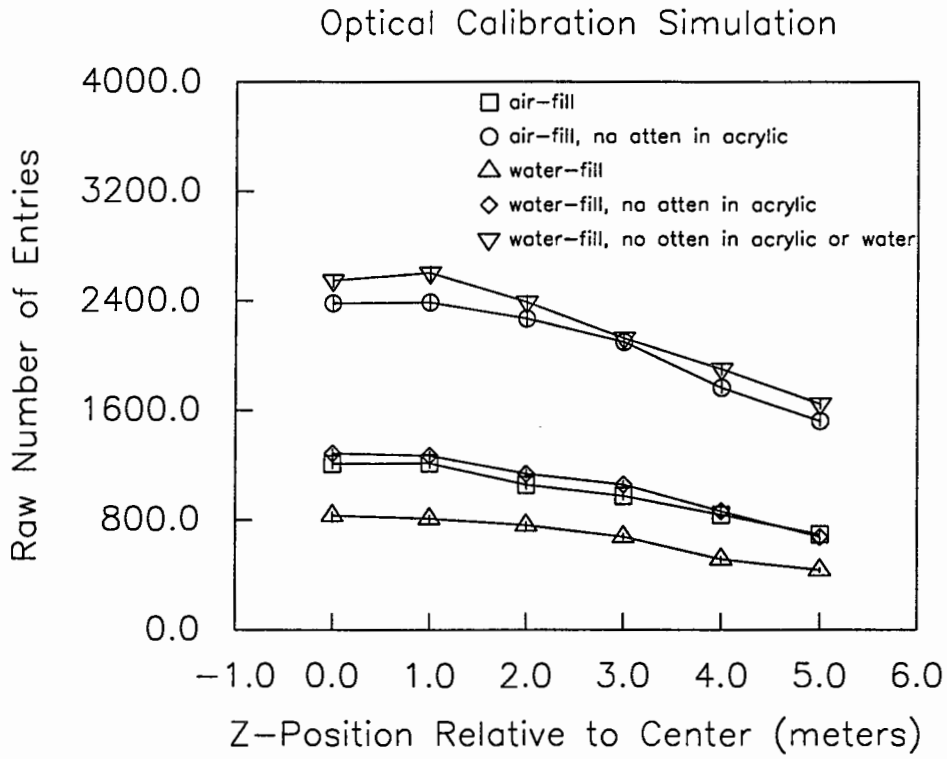

Figure 3: Total number of hits for 300 PMTs near the equator as a function of light ball position on the z axis.

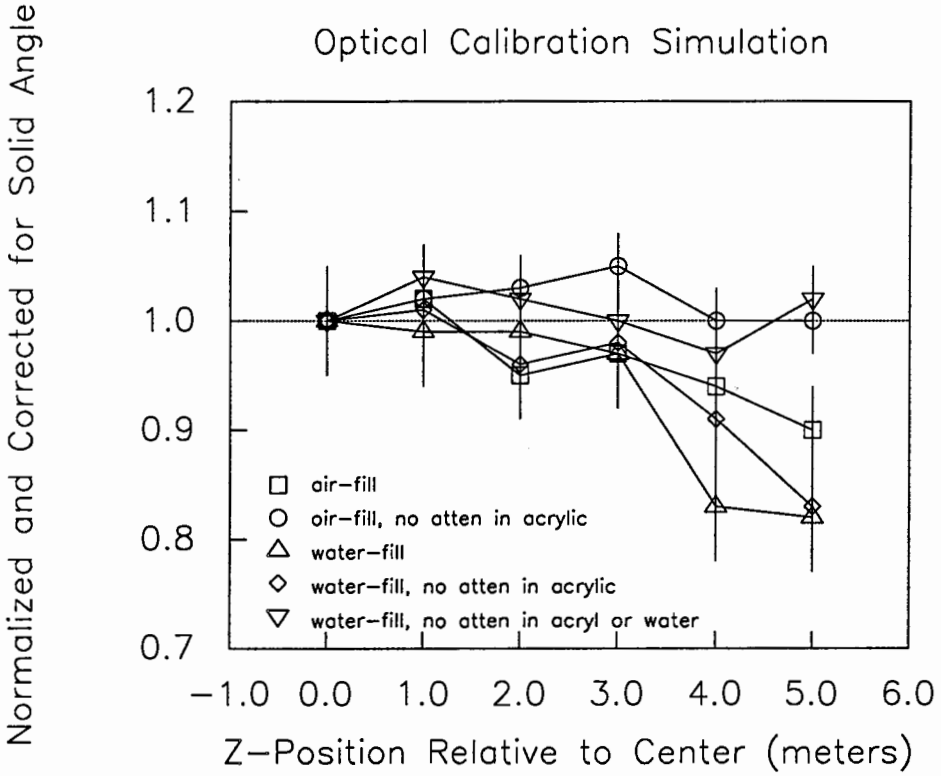

Figure 4: Same as figure 3 corrected for solid angle and normalized at z=0.

3 Detector Response to Gammas

3.1 Air Fill

3.1.1 Test of ^{16}N Calibration System

It is possible to obtain some interesting data from the ^{16}N source by using the AV to convert the 6.1 MeV gammas into electrons via Compton scattering. This applies to all triggered gamma sources, but we have only studied the ^{16}N source here. Such a run would constitute an excellent test of the whole calibration procedure, including the source deployment and the integration of the ^{16}N PMT trigger pulses into the DAQ and analysis chains. Although this might have been tested with miniSNO, it seems prudent to perform tests at Sudbury as soon as possible.

Figure 5 shows Nhit spectra for 300,000 ^{16}N decays with the standard SNOMAN ^{16}N source placed at three locations: i) center of the detector, ii) 1m directly above the bottom of the AV, and iii) 1m radially inwards from a belly plate. For these runs, events were recorded above the standard 10 Nhit DAQ threshold. It is not clear where the DAQ threshold can be set with locally triggered sources during an air fill, but a 10 Nhit threshold seems reasonable. At this threshold, 7.5% of the locally triggered ^{16}N decays would be recorded (for the source located at the AV center). The differences in Nhit spectra for the three locations simulated can be attributed to the different path lengths of acrylic that the gammas traverse. The increase in the high energy tail for the case where the ^{16}N source is 1m away from a belly plate is particularly noticeable.

Although these Nhit spectra do not show sharp features such as peaks, their relatively steep slopes at about 20-25 Nhits should allow us to calibrate the SNO Nhit energy scale. This is only possible because the ^{16}N source is locally triggered by a 2 inch PMT in the source, and this triggering has a high efficiency and a very small false trigger rate. Thus, the shape and amplitude of the Nhit spectrum, normalized to the number of source triggers, can be used to fit SNO's energy scale. Any locally triggered gamma source can be used in this way to provide an independent calibration, as long as the local trigger does not produce many false triggers.

The gamma calibrations of the Nhit energy scale can be used to infer the global absolute PMT efficiency. A few systematic errors associated with this measurement have been studied. Firstly, if the optical photon absorption lengths in the AV are changed by 50%, the ^{16}N Nhit spectrum is shifted by 10%. Thus, since these AV absorption lengths will have been separately measured to 5% accuracy (see Section 2), their contribution to the systematic uncertainty in the Nhit energy scale will be of order 1%. Secondly, the effect of pile-up from coincidences with 1.45 or 2.6 MeV gammas from the rock was studied and found to have a negligible impact on the ^{16}N Nhit spectrum, except at the very end of the high energy tail which would not, in any case, be used for this calibration. Thirdly, if the ^{16}N source trigger has a noise component which gives a false trigger rate of 5% of the true ^{16}N trigger rate, then the Nhit spectrum will be incorrectly shifted by about 2.5% in the fitting process. Lastly, the Nhit spectrum is insensitive to the source trigger efficiency as long as the there is no bias in the triggering towards different branches of the ^{16}N decay scheme. The ^{16}N source has been designed to minimize these biases and their expected contribution to the systematic error is less than 1%. Adding up all these systematic uncertainties and taking a conservative view (there are probably other significant effects which have not been considered) the overall uncertainty for measuring the PMT global absolute efficiency will be about 5%. It will be interesting to compare this measurement

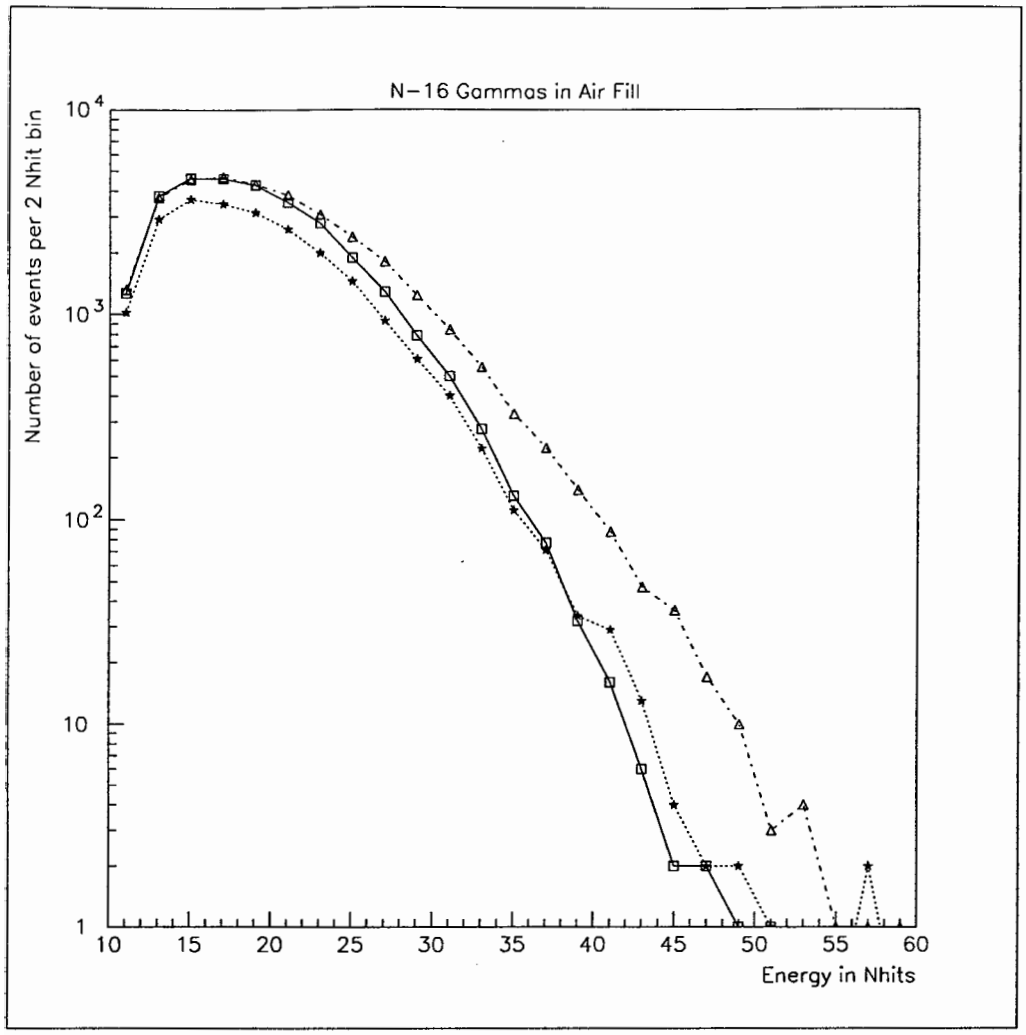

Figure 5: Energy spectrum for the ^{16}N source during air fill. Three locations for the source have been simulated: i) stars = center of detector, ii) squares = 1m from bottom of AV (z = -500cm), and iii) triangles = 1m from belly plate (x = 500cm). All curves are normalized to 300,000 decays in the source.

to that obtained from muons going through the AV (see section 4).

It should be noted that there is a further systematic error of order 5% in relating the absolute efficiency for PMTs in air to that of PMTs in water. This error stems mainly from a lack of knowledge of the photocathode thickness [2] and other details of the photocathode behaviour.

About half the ^{16}N events were fitted by the standard SNOMAN fitter with Rfit (radius of fitted vertex) less than 10m. Their Rfit distributions are shown in Figure 6 (for the same three ^{16}N source locations as in Figure 5). As expected, the distributions peak at Rfit = 600 cm, the radius of the AV. These peaks are normalized to the same number of ^{16}N decays in the source, and therefore the differences in heights are caused by two effects. The first is the different efficiencies for exceeding threshold, the second is the NHIT dependence of the fitting efficiency. Data sets like these may be very useful for understanding the behavior of fitters as they are free from scattering in the H_2O and D_2O

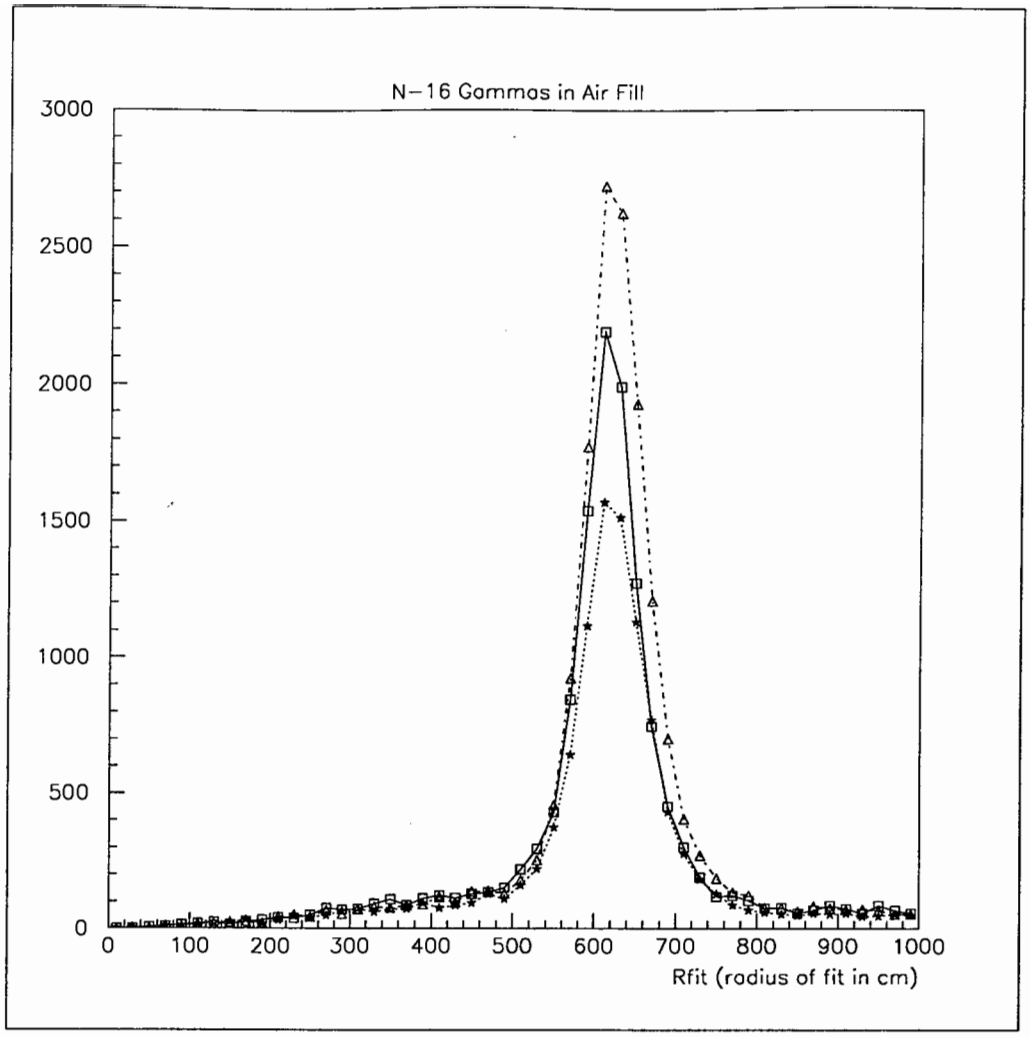

Figure 6: Rfit for the ^{16}N source during air fill. Three location for the source have been simulated: i) stars = center of detector, ii) squares = 1m from bottom of AV (z = -500cm), iii) triangles = 1m from belly plate (x = 500cm). All curves are normalized to 300,000 decays in the source.

(unfortunately not enough study has yet been done of fitter systematics to make a strong statement about what would be learned by fitting this data as opposed to fitting data in a water fill).

Table 1: Assumed gamma ray fluxes from the cavity rock

Gamma energy	Flux on AV per day
1.45	$3.0 \cdot 10^{10}$
2.6	$3.0 \cdot 10^{9}$
3.3	$1.0 \cdot 10^{8}$
5.	$1.0 \cdot 10^{6}$
7.	$2.0 \cdot 10^{5}$
9.	$1.0 \cdot 10^{4}$

3.1.2 External Gammas from the Rock

When no sources are being used, the SNO Nhit energy spectrum will be dominated by external gammas from the wall which convert through Compton scattering in the AV. This allows the possibility of using this spectrum to measure the high energy (> 4MeV) component of cavity wall gammas. These gammas are an important background for SNO even after they are attenuated by a factor of order 10^7 when the cavity is filled. The main difficulty with trying to measure their flux during the air fill stems from the huge abundance of lower energy gammas which, given the poor energy resolution of SNO during the air fill, can spill over into the high energy region of the spectrum. Other potential sources of background for this measurement are radon decays in the air and on the surface of the AV, as well as thermal neutron captures on detector materials.

The response of SNO to all of the above types of event has been simulated to see how well the high energy gammas are separated from lower energy 'background' signals. We have assumed fluxes of 2.6, 3.3, 5, 7 and 9 MeV gammas from the rock which are consistent with Refs. [3] and [1] and which are given in Table 1. The cavity will not be sealed until after the fill and so air pressure fluctuations are expected to bring 'mine' air into the cavity at a rate of 1% of the cavity volume per day [4]. This should lead to an equilibrium level of radon of 5 mBq/l, i.e. 5% of the 100 mBq/l level in mine air. We have also assumed that 1% of the radon activity in the air inside the PSUP leads to ^{214}Bi decays on the surface of the AV (from the electrostatic collection of radon daughters on the AV). Lastly, the thermal neutron flux was assumed to be $1.0 \cdot 10^{-6}$ per cm^2 per second [1].

The Nhit spectra for the low energy background signals (2.6 and 3.3 MeV gamma rays, radon decays and thermal neutrons) are shown in Figure 7, which is normalized to one day's air fill data. For the 2.6 MeV gammas we have included the effects of random coincidences between two 2.6 MeV gammas and between a 2.6 and a 1.45 MeV gamma. These 'pile-up' effects contribute to the high energy tail of the 2.6 MeV gamma signal.

In Figure 7 the sum of all the low energy spectra from Figure 8 is compared to the spectra of the high energy gammas (5, 7, and 9 MeV), again normalized to one day's air fill data. It is clear from this figure that it will be very hard to disentangle the high energy gammas from the tail of the low energy background signals. However, things can

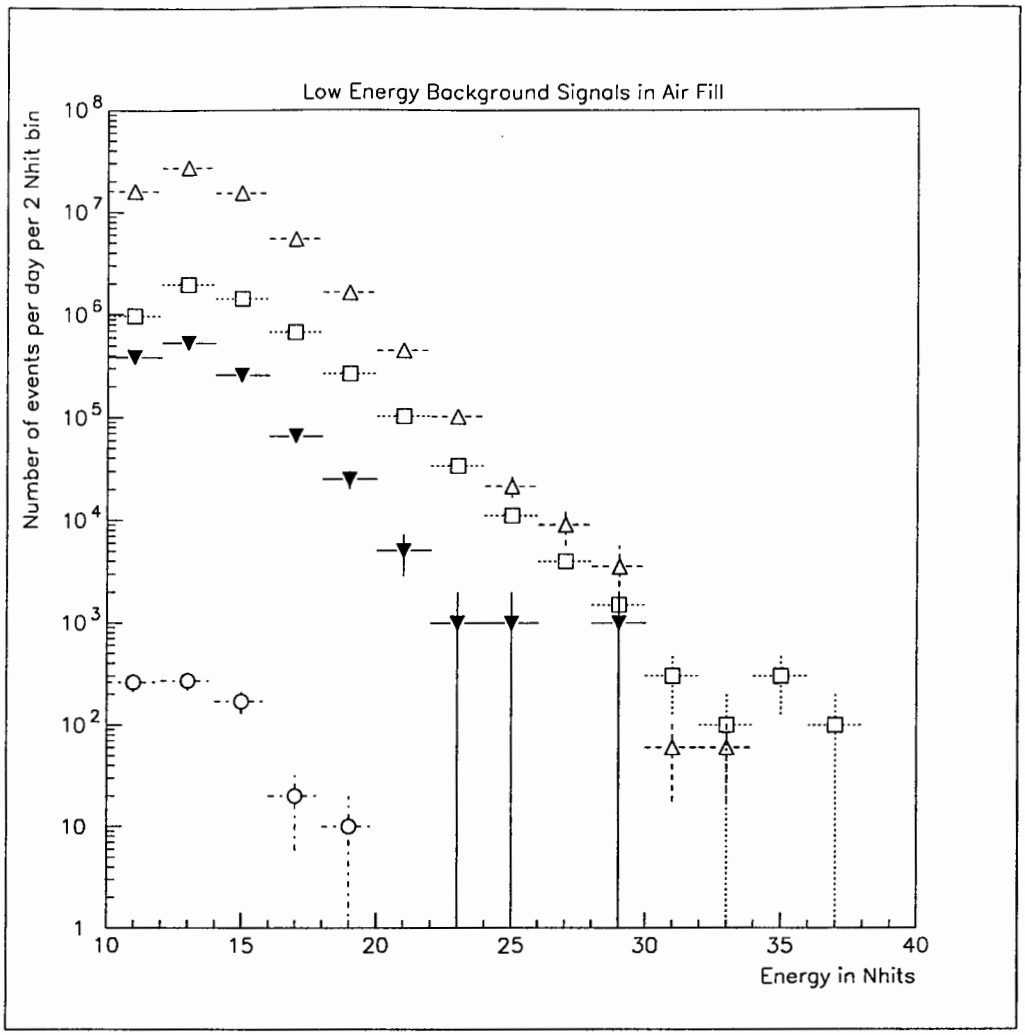

Figure 7: Low energy background signals during the air fill. The symbols are as follows: i) open triangles – 2.6 MeV gammas (including pile-up with 1.45 MeV and 2,6 MeV gammas), ii) open squares – 3.3 MeV gammas, iii) solid triangle – ^{214}Bi decays from radon in the air and on the surface of the AV, and iv) open circles – thermal neutron captures on detector materials.

be improved a little by making some cuts on the data, i.e. requiring events to reconstruct within 1m of the AV (500cm < Rfit < 700cm) and excluding the equatorial region which contains the belly plates (abs(Zfit) > 200cm). These cuts make the high energy gammas slightly better separated from the tail of the low energy signals, as can be seen in Figures 9 and 10. Even so, only the 7 MeV gamma component seems to stick out sufficiently to be accessible in this data.

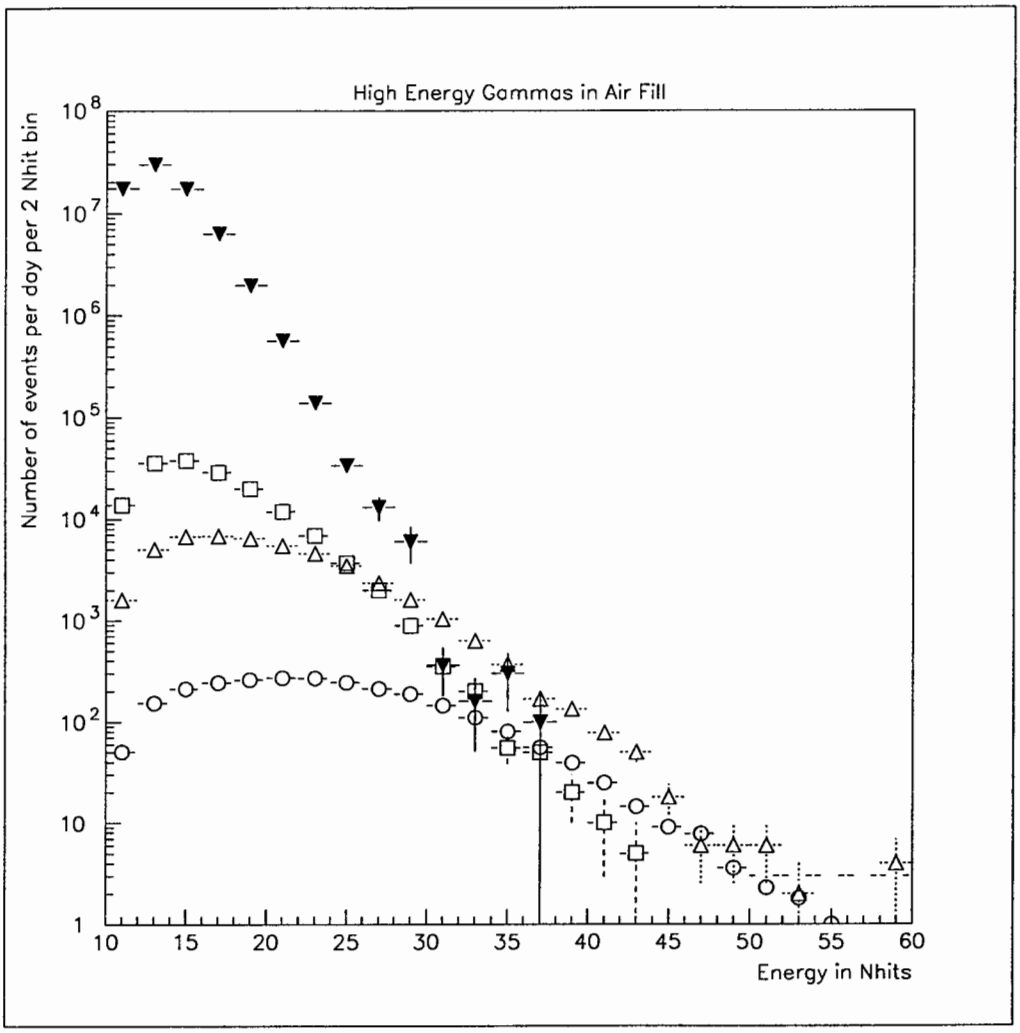

Figure 8: High energy gammas and low energy background during the air fill. The symbols are as follows: i) solid triangles – low energy background (sum of spectra shown in Figure 7, ii) open squares – 5 MeV gammas, iii) open triangle – 7 MeV gammas, and iv) open circles – 9 MeV gammas.

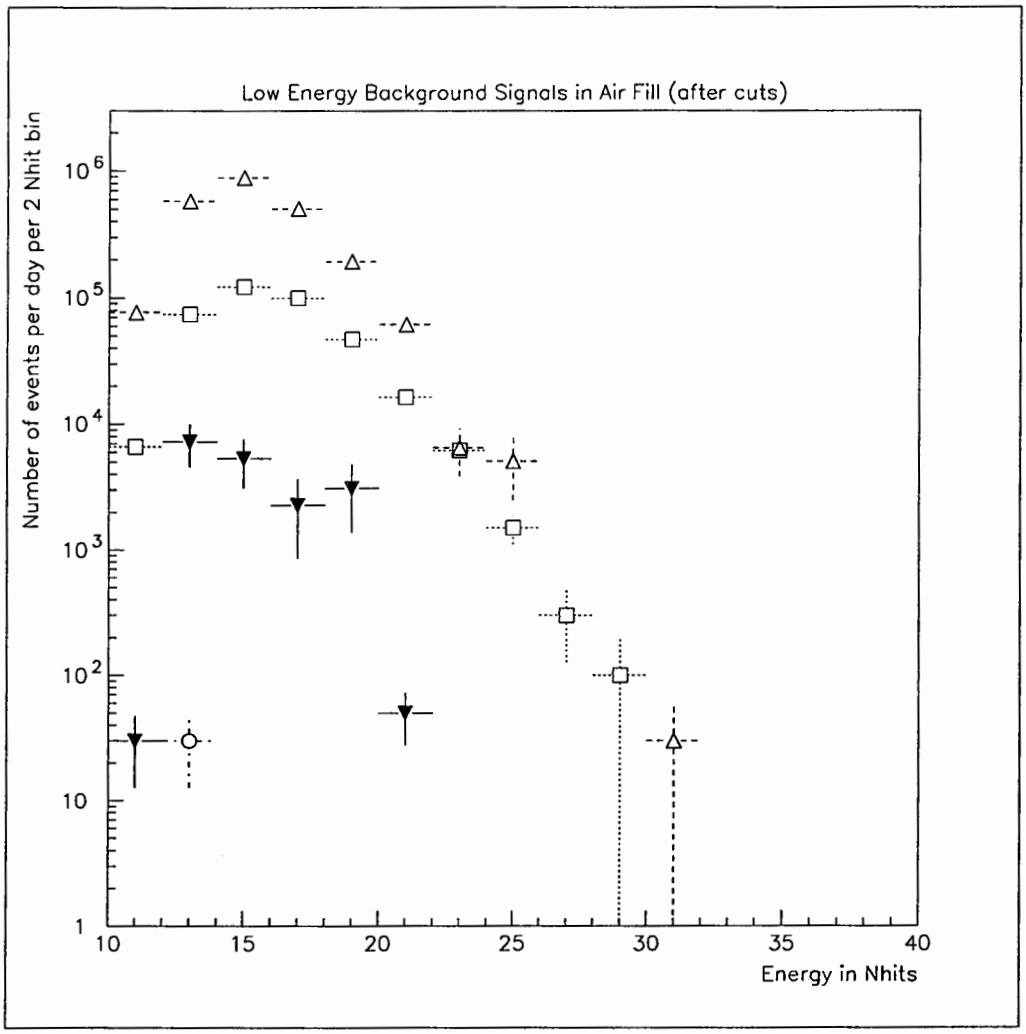

Figure 9: Low energy background signals during the air fill after the cuts discussed in the text. The symbols are as follows: i) open triangles – 2.6 MeV gammas (including pile-up with 1.45 MeV and 2,6 MeV gammas), ii) open squares – 3.3 MeV gammas, iii) solid triangle – ^{214}Bi decays from radon in the air and on the surface of the AV, and iv) open circles – thermal neutron captures on detector materials.

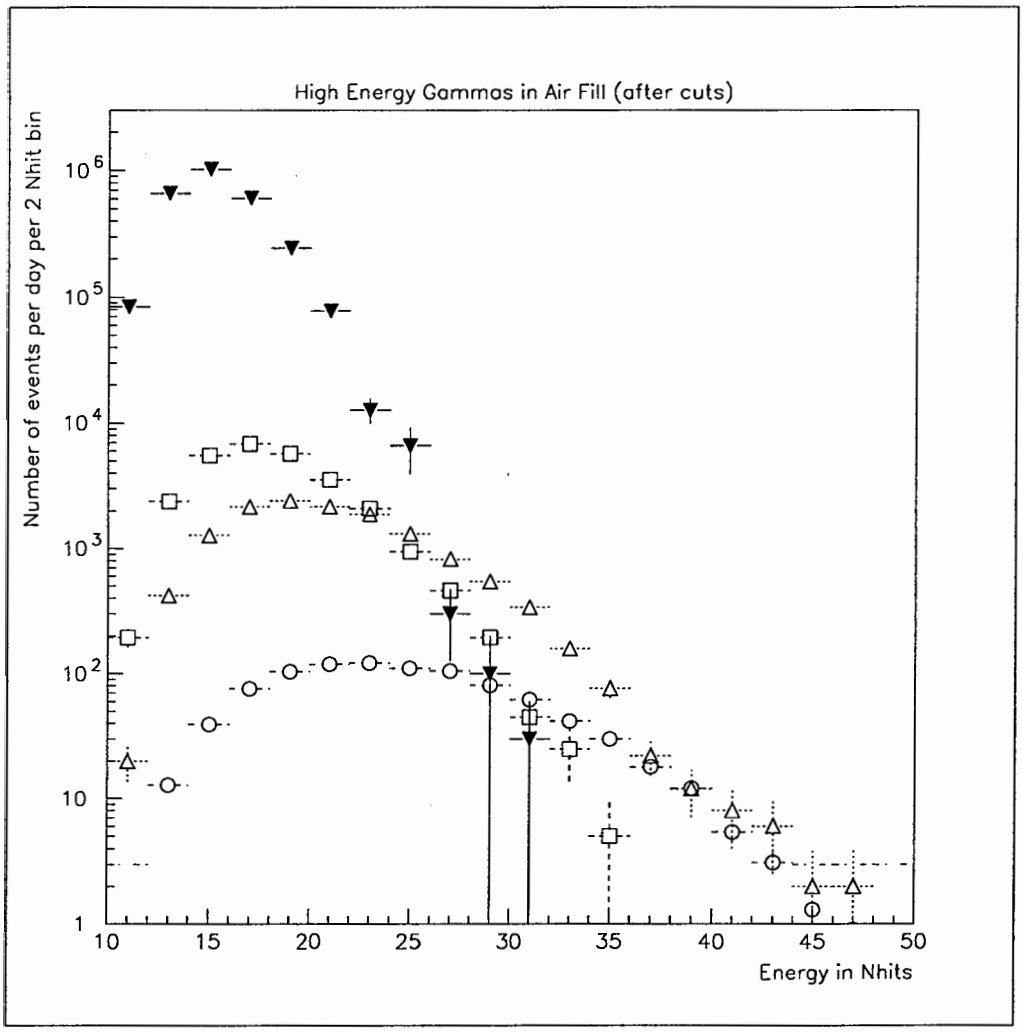

Figure 10: High energy gammas and low energy background during the air fill after the cuts discussed in the text. The symbols are as follows: i) solid triangles – low energy background (sum of spectra shown in Figure 9), ii) open squares – 5 MeV gammas, iii) open triangle – 7 MeV gammas, and iv) open circles – 9 MeV gammas.

3.2 Half Fill

As SNO is being filled with water it will become a better converter of gammas and thus its energy resolution will improve. This will make it easier to separate the high energy gammas from the tails of lower energy signals. As an example, we have considered a half-filled detector where the D_2O level is at the equator of the AV and the H_2O level is 60 cm higher.

3.2.1 ^{16}N Calibration Source

With this half-filled detector we have simulated the ^{16}N calibration source at two locations: i) immersed at z = -300 cm, to study fully converted gammas, and ii) above the D_2O at z = 500 cm, to study external gammas incident on the D_2O and H_2O. The Nhit spectra for these two cases are shown in Figure 11. The immersed source gives a broad peak at about 50 Nhits which corresponds to fully converted 6.1 MeV gammas. The source located above the D_2O shows the same peak at 50 Nhits from gammas incident on the D_2O or H_2O which are essentially fully converted. As expected, the amplitude of this peak relative to the ^{16}N local trigger rate is reduced by a factor given by the fraction of solid angle that the D_2O and H_2O subtend from this source location. A lower Nhit 'peak' from gammas converting in the top half of the AV is also found for the source above the D_2O.

Figure 12 shows the distributions of Zfit, the fitted z coordinate, for our two source locations. The peak at Zfit=0 (the D_2O level), for the source placed above the D_2O, correlates with the peak at 50 Nhits for fully converted gammas and the events with ZFit > 200 cm are low in Nhits, as expected for gammas converting in the AV. The 'double-peak' in Zfit for the immersed source is caused by downward going gammas reconstructing just below the source location (-300cm) and upward going gammas having their reconstructed vertices 'pulled' upwards by about 100cm from mirror effects at the D_2O/air interface.

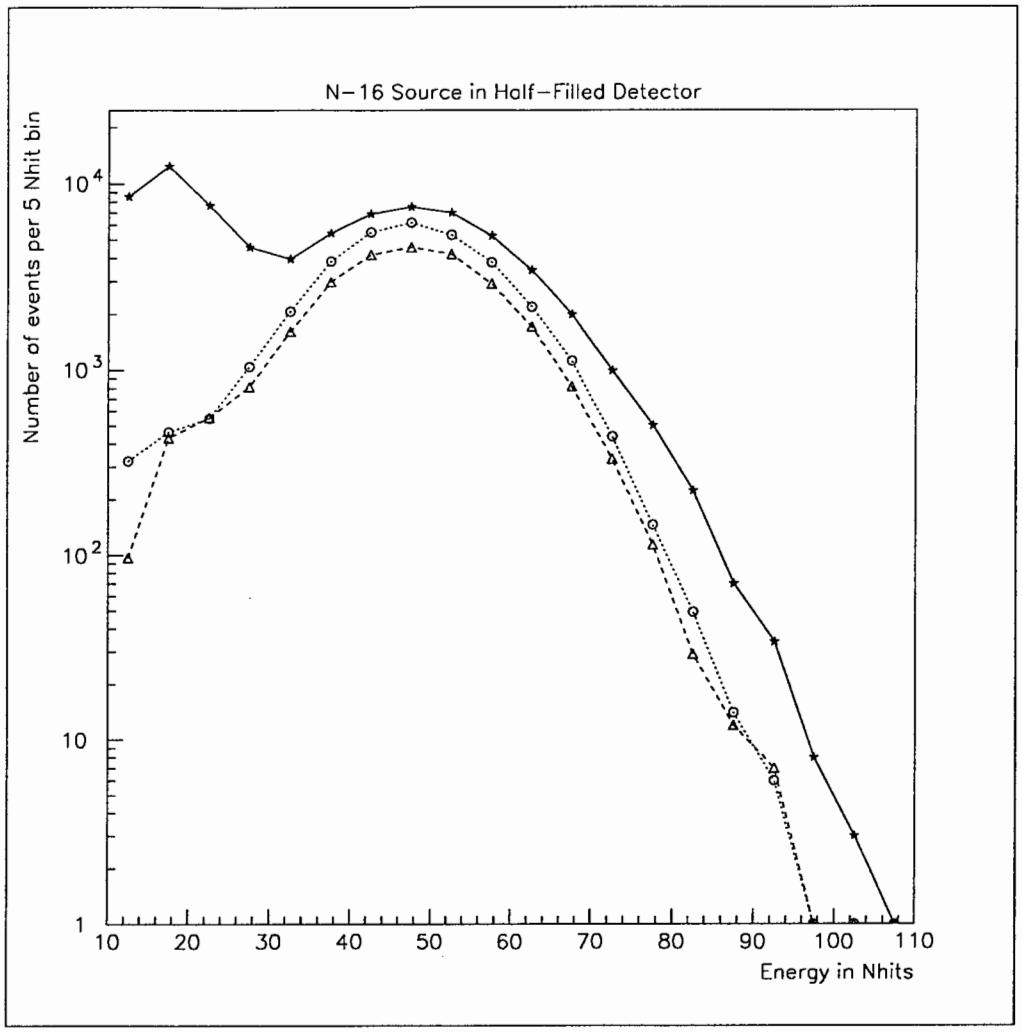

Figure 11: Energy spectrum for the ^{16}N source with a half-filled detector. Two locations for the source have been simulated: i) stars = 5m above the surface of the D_2O (z = 500cm) to study the response of external gammas (300,000 ^{16}N decays generated), and ii) circles = immersed 3m below the surface of the D_2O (z = 300cm) to study fully converted gammas (50,000 ^{16}N decays generated). The triangles represent the same location as i) after the following cuts: abs(Zfit) < 200cm and Rfit < 500cm (see text).

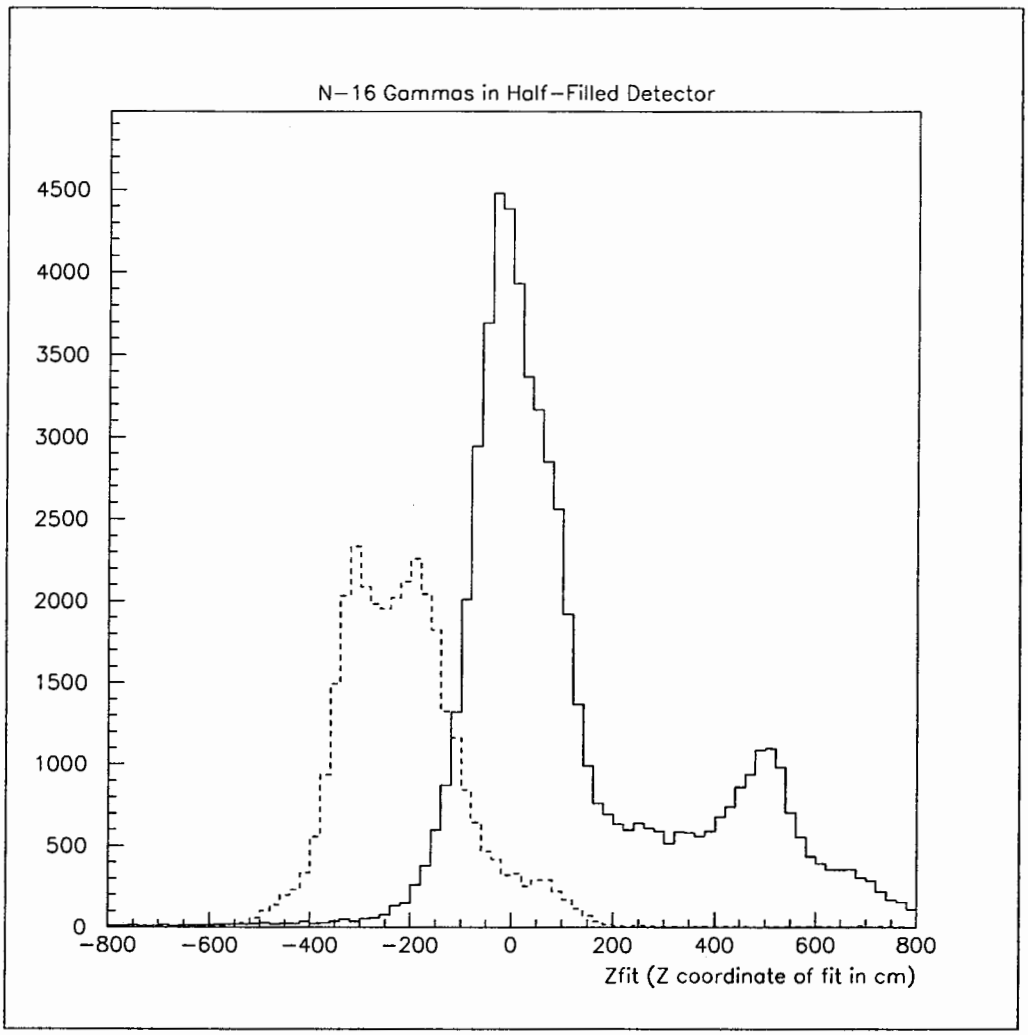

Figure 12: Zfit distribution for the ^{16}N source with a half-filled detector. Two locations for the source have been simulated: i) solid line = 5m above the surface of the D_2O (z = 500cm) to study the response of external gammas (300,000 ^{16}N decays simulated), and ii) dashed line = immersed 3m below the surface of the D_2O (z = -300cm) to study fully converted gammas (50,000 decays simulated). For case i) the peak at z = 0 cm is due to gammas converting near the surfaces of the D_2O and H_2O and the events above 200 cm are conversion in the AV. For case ii) the peak just below the source location (z = -300cm) is from downward gammas and the peak at -200cm is from upward gammas which have been 'pulled' towards the D_2O/air interface by reflections at this surface.

3.2.2 External Gammas

To simulate rock gammas during the half fill, gammas were generated from the top half of the cavity towards the PSUP. Thus the assumed rates of gammas were the same as in Table 1, since the PSUP has twice the area as the AV but we are only concerned with gammas from the top half of the cavity. In addition to gammas, thermal neutrons were generated at the same flux as for the air fill ($1.0 \cdot 10^{-6}$ per cm^2 per s) and ^{214}Bi events were generated in the H_2O and D_2O to account for radon levels during the fill. We have assumed that the concentration of radon in the D_2O and H_2O will be 1 mBq/l, i.e. one hundred times less than the 0.1 Bq/l of mine air and 10^4 times more than the D_2O target of 10 decays per day per tonne. This is a conservative assumption given that the expected equilibrium level for cavity air during the fill is 5 mBq/l (see section 3.1.2), and that only a small fraction of this radon should get through the (expected) stagnant layer of cool air above the D_2O and H_2O [4].

The Nhit spectra for the low energy background signals (2.6 and 3.3 MeV gammas, radon and thermal neutrons) are shown in Figure 13. Radon contributes less to the background than the low energy external gammas from the wall. Thermal neutrons result in a peak at about 50 Nhits from capture on deuterium, but this peak does not stick out above the tail from the external gamma events.

In Figure 14 the sum of all the background spectra from Figure 13 is plotted against the high energy gammas (5, 7 and 9 MeV). It is clear from Figure 14 that the high energy gammas stick out above the 'background' above 55 Nhits. This is a much better separation than shown in Figures 8 and 10 for the air fill. It should be noted that with the DAQ's maximum continuous acquisition rate of about 1 kHz (10^8 events per day), the threshold will have to be shifted to 20 or even 30 Nhits to avoid excessive dead time.

Two cuts can be placed on external gamma events to improve their energy resolution and hence make the separation of the different signals in Figure 14 cleaner. The first cut, abs(Zfit)$<$ 200 cm, removes the low energy component from gammas which convert on the AV, and the second cut, Rfit $<$ 500 cm removes events which convert in the H_2O and which dominate the high energy tail of the resolution function since they can have very little light attenuation in the AV. The effect of these two cuts on the energy resolution can be seen in Figure 5, where the energy spectrum (after cuts) for the N-16 source located above the D_2O looks very close to the energy spectrum for the immersed N-16 source.

Figures 15 and 16 show the effect of these cuts on the low energy background signals and high energy external gammas, respectively. There is some improvement in the energy resolution which should make it easier to separate the different signals. This is most noticeable for the 5 and 9 MeV external gammas. This is dependent on our understanding the resolution function and fitter systematics in the half-filled configuration (which corresponds to having a partial mirror halfway up the cavity). SNO should therefore plan on spending a few days with calibration sources in place during filling. It is difficult to anticipate exactly with what uncertainty the flux of high energy rock gammas could be measured from the spectra shown in Figures 16 and 14, but at most a factor two uncertainty seems reasonable, particularly with the availability of the ^{16}N source as a means of calibrating this spectrum. Further simulations need to be run to decide whether comparing data from different fill levels will add to our ability to determine the external gamma background.

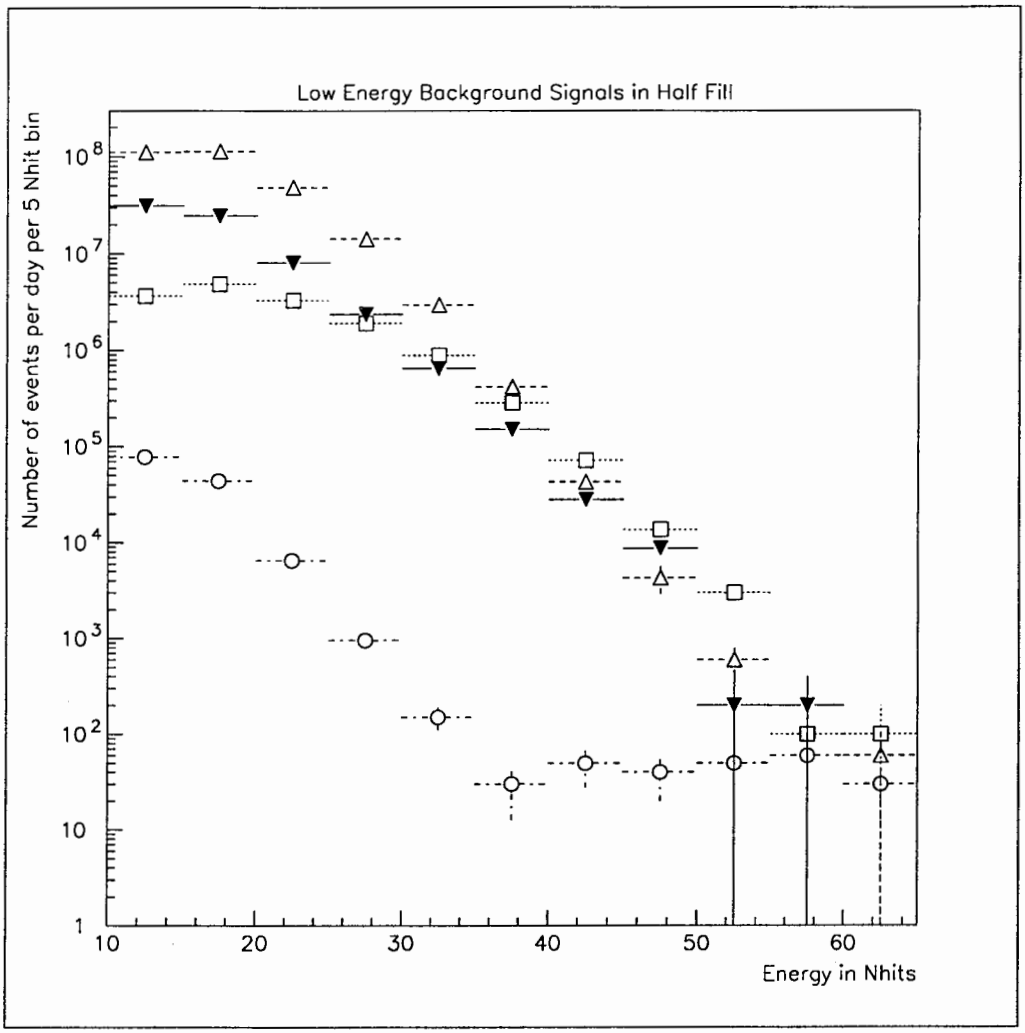

Figure 13: Low energy background signals during the half fill. The symbols are as follows: i) open triangles – 2.6 MeV gammas (including pile-up with 1.45 MeV and 2,6 MeV gammas), ii) open squares – 3.3 MeV gammas, iii) solid triangle – ^{214}Bi decays from radon in the H_2O and D_2O, and iv) open circles – thermal neutron captures on detector materials.

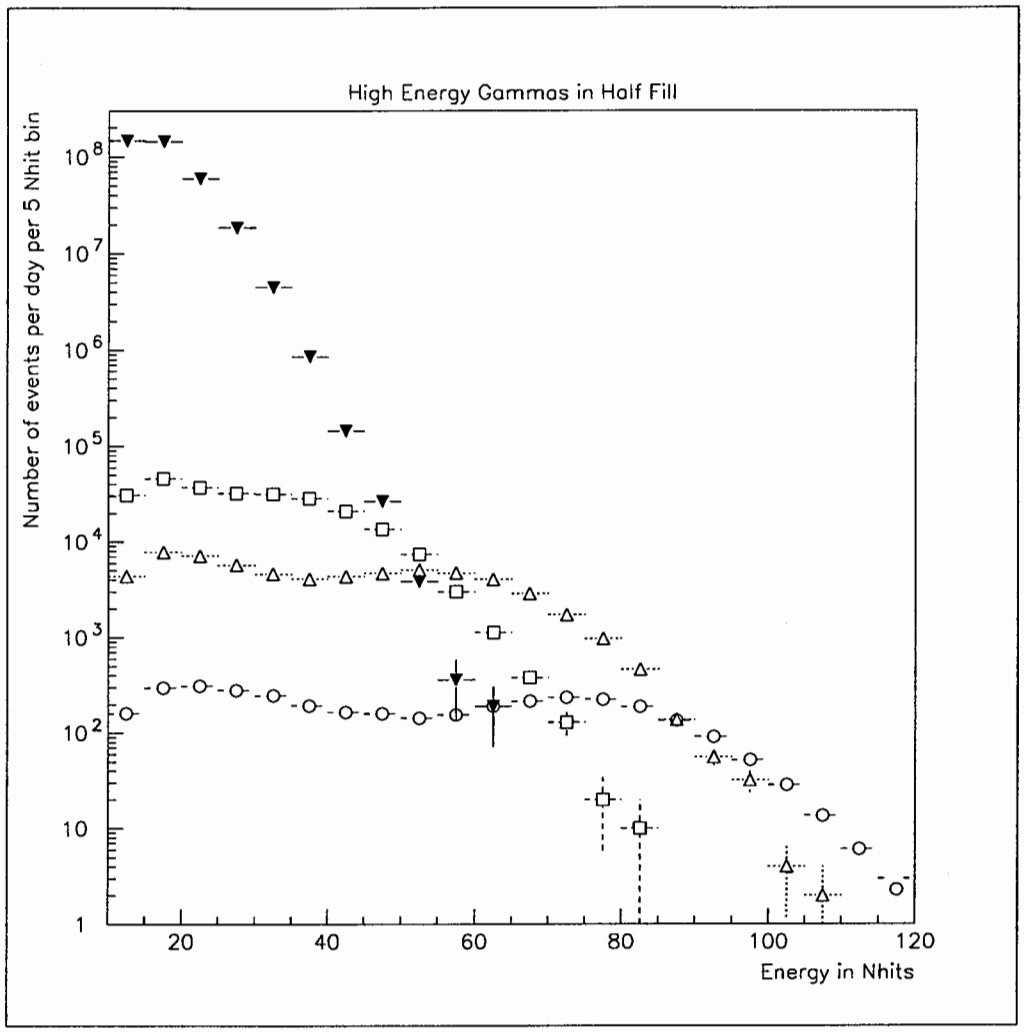

Figure 14: High energy gammas and low energy background during the half fill. The symbols are as follows: i) solid triangles – low energy background (sum of spectra shown in Figure 13, ii) open squares – 5 MeV gammas, iii) open triangle – 7 MeV gammas, and iv) open circles – 9 MeV gammas.

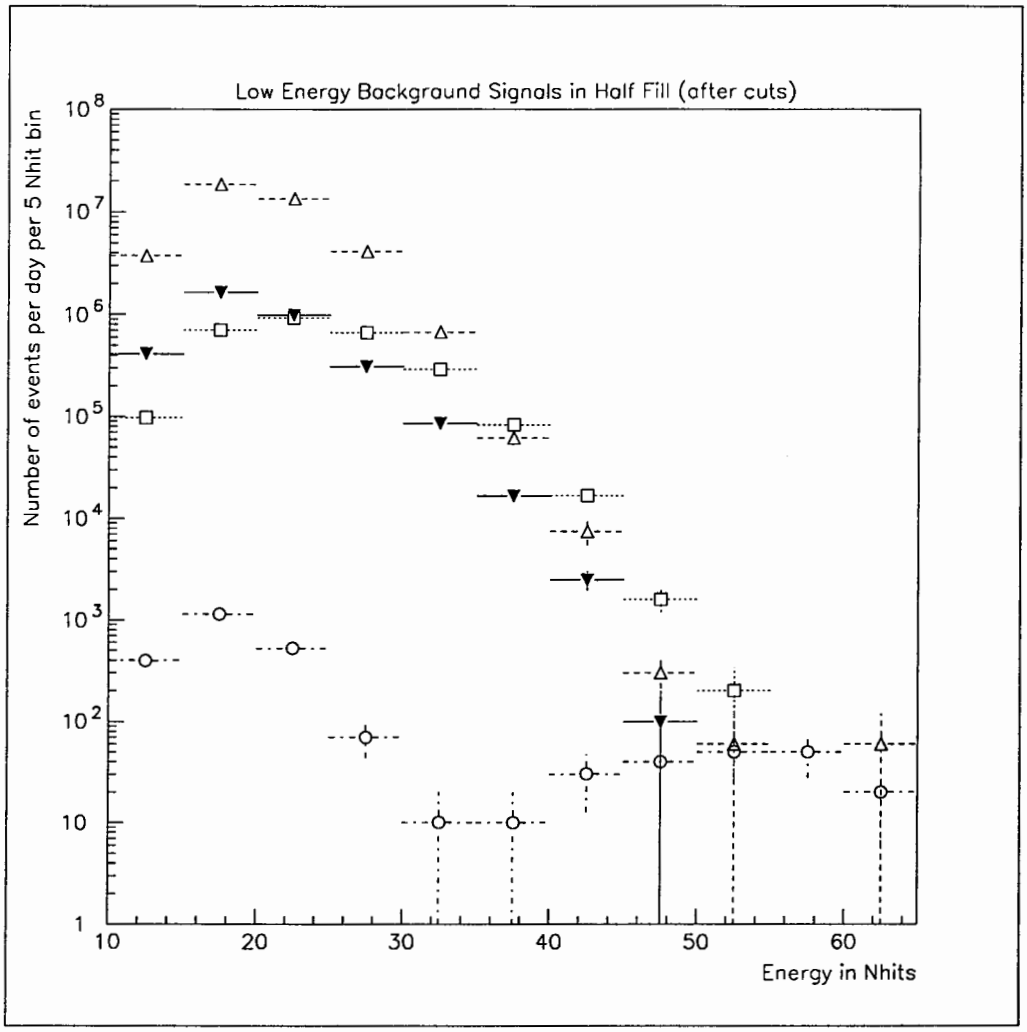

Figure 15: Low energy background signals during the half fill after the cuts described in the text. The symbols are as follows: i) open triangles – 2.6 MeV gammas (including pile-up with 1.45 MeV and 2,6 MeV gammas), ii) open squares – 3.3 MeV gammas, iii) solid triangle – ^{214}Bi decays from radon in the H_2O and D_2O, and iv) open circles – thermal neutron captures on detector materials.

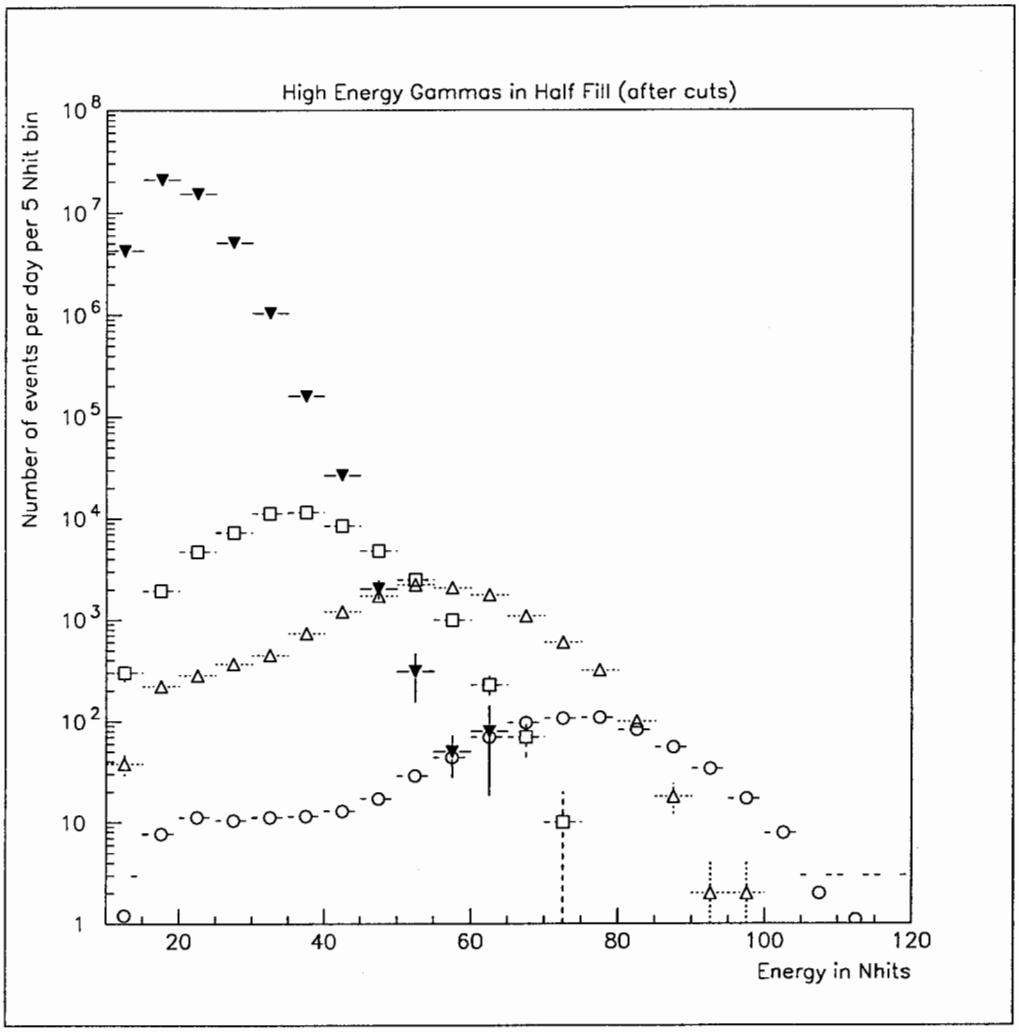

Figure 16: High energy gammas and low energy background during the half fill after the cuts described in the text. The symbols are as follows: i) solid triangles – low energy background (sum of spectra shown in Figure 15, ii) open squares – 5 MeV gammas, iii) open triangle – 7 MeV gammas, and iv) open circles – 9 MeV gammas.

4 Detector Response to Muons

The only significant source of large NHIT (> 100) background events during airfill is the underground muon flux. Simulations indicate that these events will offer, perhaps somewhat surprisingly, a good test of the photon transport routines in SNOMAN. They should also offer a calibration of the absolute photon counting efficiency of the SNO detector.

The sensitivity of the hit patterns produced by through muons in an air fill to details of the optical transport can be appreciated by looking at Figure 17. This shows the hit pattern produced by one of 1100 muons simulated penetrating a sphere at 900 cm radius (about ten days worth of events at the SNO rate as roughly predicted from the flux in Gaisser's book[5]). The dots show the PMT locations, the heavy circles show the path of the muon through the detector, and the stars show the positions of the hit photomultipliers. Three features which are present in almost all the hit patterns for airfill muons are seen in this plot: 1) a crescent of hits produced from the Čerenkov light created by the muon on its first passage through the AV (a crescent rather than a circle because the muon is not travelling normal to the surface of the AV, therefore part of the light is trapped in the AV by total internal reflection); 2) a similar crescent from light produced when the muon goes through the AV the second time; and 3) a small cluster of tubes with very high charge deposits where the muon exits the PSUP (this region is obscured on this plot by the muon track but consists of 8 adjacent tubes). All these features depend on the detailed simulation of photon transport in SNO, so airfill data on such events would provide a test of the simulation using photons actually generated within the AV (which is not possible using the light ball discussed above). As such it is complementary to the test using the ^{16}N source near the AV discussed above, but requires less effort.

A more interesting test is perhaps available from looking at all muon events produced over a period of time. Muons were simulated with an energy spectrum uniform from 1 to 100 GeV and an angular distribution given by a Gaussian with a sigma of 12 degrees centered on 23 degrees. These are reasonable imitations of the distributions shown in figures 6.4 and 6.5 of Gaisser's book[5], but the correlations between angle and energy have not yet been modelled (this should not effect the conclusions below). The NHIT spectrum produced by 1100 events crossing an upper half-sphere at 900 cm. is shown in Figure 18. The peak at low NHIT (centroid $\approx$17 hits) is due to muons which miss the AV. These will not be seen beneath the external gamma ray background described above. The second peak at NHIT of about 120 is more interesting. This is primarily due to Čerenkov photons created by muons traversing the AV. This is indicated by the crescents seen in Figure 17, but a stronger test was made by repeating the simulation with all sources of light other than muon Čerenkov radiation turned off. The result is shown in Figure 19, where the peak from the full muon simulation is superposed with the one with only muon Čerenkov light. When the full simulation is used the mode of the peak shifts up by only about 10%, while the tail increases considerably (due to Moller scattered electrons in the AV).

This opens the possibility of using the position of this peak as a measurement of the absolute photon counting efficiency of the SNO detector during an air fill. The peak is clearly visible in a single day's simulated data with a statistical uncertainty of only about 4% in its position. In order to argue that the position of this peak could be used to constrain the number of hits per MeV in SNO one would have to argue that the number of photons produced is well understood and that there are not substantial uncertainties in their transport that do not effect other events. The number of Čerenkov photons produced

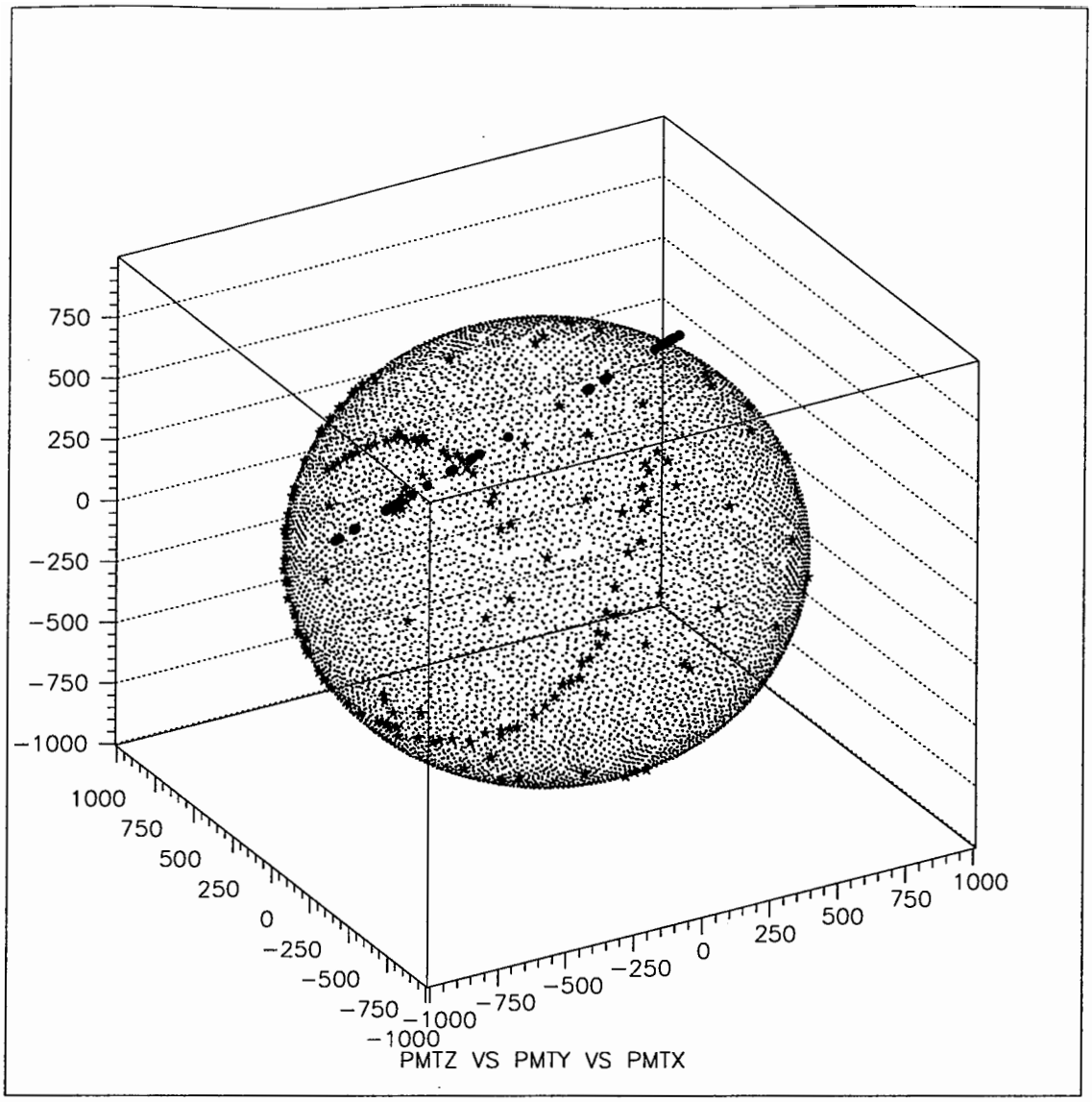

Figure 17: The hit pattern produced by a muon passing through the AV during an air fill. The dots show the PMT positions, the stars the hit PMT's, and the solid circles mark the track of the muon.

directly by a muon per unit track length can be estimated with negligible uncertainty. We assume that the 10% shift mentioned above in the position of the peak coming from physics processes other than muon Čerenkov can be modelled to at least the 25% level. That would produce an uncertainty comparable to the statistical uncertainty if we take 10 days of such air fill data (the most we can imagine that we will take barring problems with starting the water systems). The number of hits produced scarcely correlates with the muon energy (since most of the light is from Čerenkov , which is independent of energy at these energies), so uncertainties in the muon energy spectrum should not be significant. Muons were also simulated originating 2 meters back in the rock wall to see if showering in the rock would produce radiation accompanying the muons sufficient to wash out the peak. The peak shifted up by about 5% in these simulations, indicating that this effect must be taken into

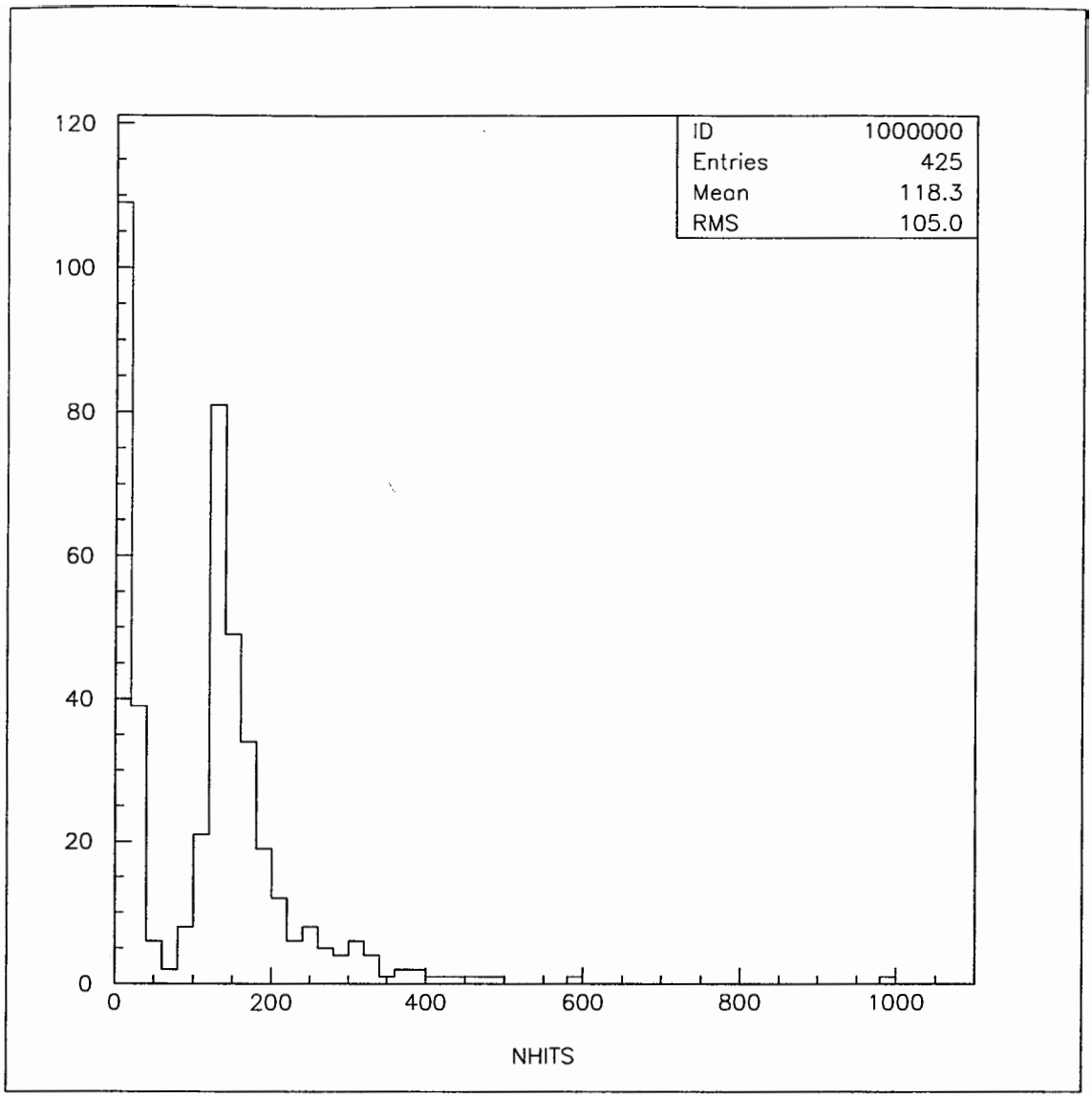

Figure 18: Raw NHIT spectrum from 1100 simulated muons crossing a sphere at 900 cm. during an air fill.

account but should not seriously limit the accuracy of such a measurement. Changing the sigma of the angular distribution to 17 degrees produced a 3% change in the peak position, so uncertainties in the angular distribution should also not create a substantial uncertainty in the measurement. Increasing the attenuation length in the acrylic by 5% made a 2.5% change in the position of the peak, so given the measurements discussed above this would not produce a significant uncertainty. Imperfections in the AV surface were modelled by producing a 10% diffuse scattering probability for all photons crossing an air/acrylic interface. This did not affect the peak position within errors (some photons that would have been trapped by total internal reflection could now escape the AV, some that would have escaped were now trapped, apparently these effects approximately cancelled). From the simulations we have made and the systematics we have considered we are therefore unable to find any reason why a measurement of the absolute photon counting efficiency

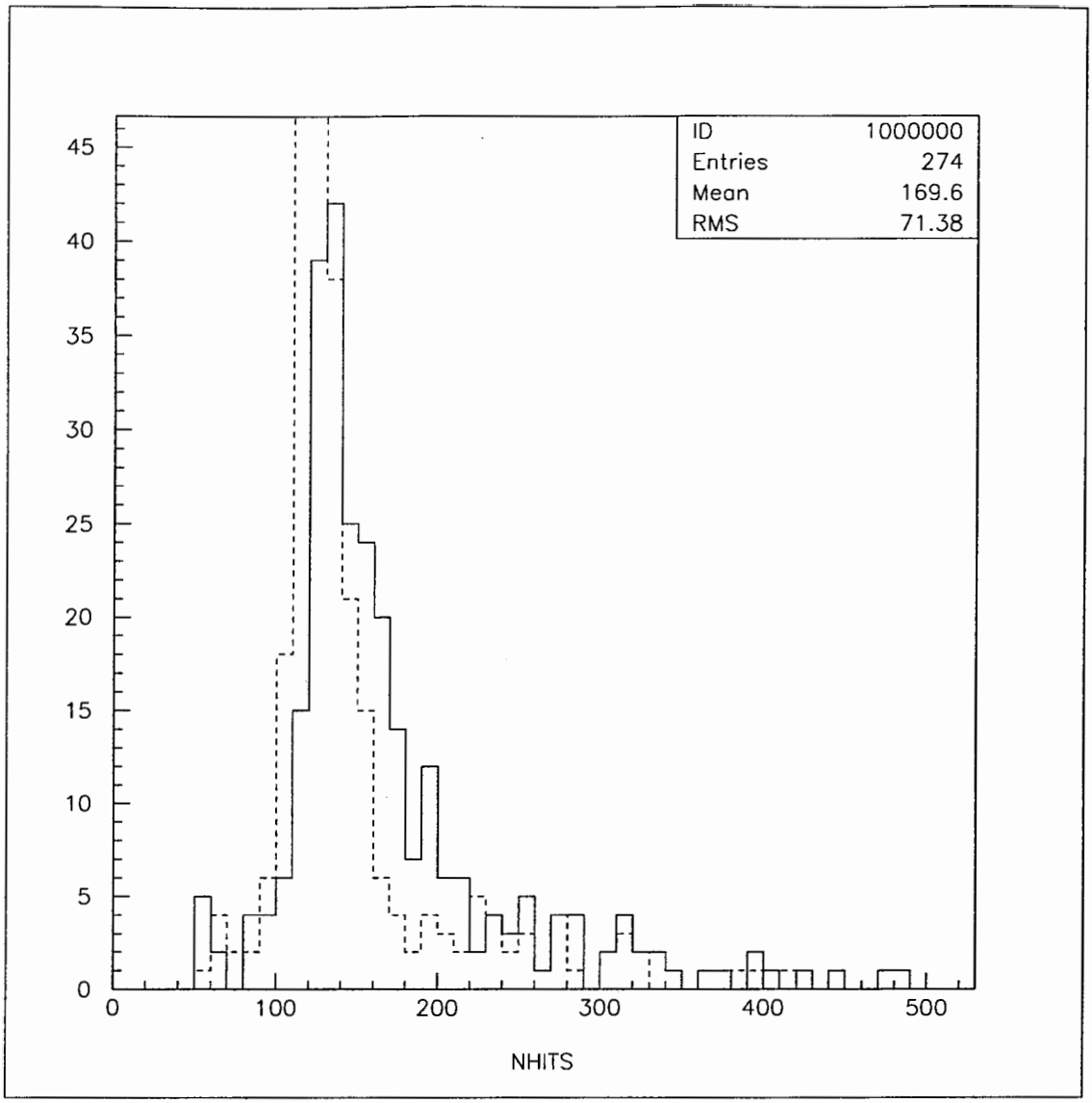

Figure 19: Peak in the NHIT distribution caused by muons crossing the AV with full simulation (solid line) and only Čerenkov light (dashed curve).

in SNO accurate at about the 5% level could not be made from observing muons in air. As mentioned in the conclusions section, there is an additional 5% uncertainty in relating this to the absolute photon counting efficiency in water which arises from our understanding of the photocathode[2].

References

[1] M.C. Perillo Isaac *et al.*, "High Energy Gamma-Rays Measurements in the SNO Cavity", SNO-STR-97-??

[2] M.E. Moorhead and N.W. Tanner, *Nucl. Inst. MethsA* **378**, 162 (1996).

[3] P. Skensved and B.C. Robertson, "Summary of Backgrounds in SNO", SNO-STR-94-13.

[4] D. Sinclair, private communication.

[5] T.K. Gaisser, *Cosmic Rays and Particle Physics*, Cambridge University Press, 1990.